BRAIN
A JOURNAL OF NEUROLOGY

Magnetic resonance imaging evidence for presymptomatic change in thalamus and caudate in familial Alzheimer's disease

Natalie S. Ryan,[1] Shiva Keihaninejad,[1,2] Timothy J. Shakespeare,[1] Manja Lehmann,[1] Sebastian J. Crutch,[1] Ian B. Malone,[1] John S. Thornton,[3,4] Laura Mancini,[3,4] Harpreet Hyare,[5] Tarek Yousry,[3,4] Gerard R. Ridgway,[1,6] Hui Zhang,[2] Marc Modat,[1,2] Daniel C. Alexander,[2] Martin N. Rossor,[1] Sebastien Ourselin[1,2] and Nick C. Fox[1]

1 Dementia Research Centre, Department of Neurodegenerative Disease, University College London (UCL) Institute of Neurology, Queen Square, London, WC1N 3BG, UK
2 Centre for Medical Image Computing, UCL, Malet Place, London, WC1E 6BT, UK
3 Lysholm Department of Neuroradiology, National Hospital for Neurology and Neurosurgery, UCLH NHS Foundation Trust, Queen Square, London, WC1N 3BG, UK
4 Neuroradiological Academic Unit, UCL Institute of Neurology, Queen Square, London, WC1N 3BG, UK
5 MRC Prion Unit, Department of Neurodegenerative Disease, UCL Institute of Neurology, Queen Square, London, WC1N 3BG, UK
6 Wellcome Trust Centre for Neuroimaging, UCL Institute of Neurology, Queen Square, London, WC1N 3BG, UK

Correspondence to: Natalie S Ryan,
Dementia Research Centre,
Box 16 National Hospital for Neurology and Neurosugery,
Queen Square,
London WC1N 3BG, UK
E-mail: natalie.ryan@ucl.ac.uk

Amyloid imaging studies of presymptomatic familial Alzheimer's disease have revealed the striatum and thalamus to be the earliest sites of amyloid deposition. This study aimed to investigate whether there are associated volume and diffusivity changes in these subcortical structures during the presymptomatic and symptomatic stages of familial Alzheimer's disease. As the thalamus and striatum are involved in neural networks subserving complex cognitive and behavioural functions, we also examined the diffusion characteristics in connecting white matter tracts. A cohort of 20 presenilin 1 mutation carriers underwent volumetric and diffusion tensor magnetic resonance imaging, neuropsychological and clinical assessments; 10 were symptomatic, 10 were presymptomatic and on average 5.6 years younger than their expected age at onset; 20 healthy control subjects were also studied. We conducted region of interest analyses of volume and diffusivity changes in the thalamus, caudate, putamen and hippocampus and examined diffusion behaviour in the white matter tracts of interest (fornix, cingulum and corpus callosum). Voxel-based morphometry and tract-based spatial statistics were also used to provide unbiased whole-brain analyses of group differences in volume and diffusion indices, respectively. We found that reduced volumes of the left thalamus and bilateral caudate were evident at a presymptomatic stage, together with increased fractional anisotropy of bilateral thalamus and left caudate. Although no significant hippocampal volume loss was evident presymptomatically, reduced mean diffusivity was observed in the right hippocampus and reduced mean and axial diffusivity in the right cingulum. In contrast, symptomatic mutation carriers showed increased mean, axial and in particular radial diffusivity, with reduced fractional anisotropy, in all of the white matter tracts of interest. The symptomatic group also showed atrophy and increased mean diffusivity in all of the subcortical grey matter regions of interest, with increased fractional anisotropy in bilateral putamen. We propose that axonal

injury may be an early event in presymptomatic Alzheimer's disease, causing an initial fall in axial and mean diffusivity, which then increases with loss of axonal density. The selective degeneration of long-coursing white matter tracts, with relative preservation of short interneurons, may account for the increase in fractional anisotropy that is seen in the thalamus and caudate presymptomatically. It may be owing to their dense connectivity that imaging changes are seen first in the thalamus and striatum, which then progress to involve other regions in a vulnerable neuronal network.

Introduction

Alzheimer's disease affects an estimated 24 million people worldwide and, unless more effective treatments are developed, this figure is predicted to double every two decades (Ferri *et al.*, 2005). A small minority of cases are caused by autosomal dominantly inherited mutations in the presenilin 1 (*PSEN1*), presenilin 2 (*PSEN2*) or amyloid precursor protein (*APP*) genes, or by *APP* duplications. Although rare, these mutations show virtually complete penetrance and mutation carriers therefore provide a unique opportunity to gain insights into the earliest stages of the disease. A wealth of evidence now indicates that the symptoms of Alzheimer's disease are preceded by a long period of gradual accrual of pathological change (Price and Morris, 1999; Bateman *et al.*, 2012). The disappointing results of trials of putative disease-modifying therapies in established Alzheimer's disease have shifted attention towards starting treatment earlier in the disease course. Familial Alzheimer's disease mutation carriers represent a cohort in whom treatment could be initiated at a presymptomatic stage and a number of such trials are currently being designed (Reiman *et al.*, 2010; Bateman *et al.*, 2011). As the individuals participating in these trials will have little or no cognitive impairment, there is a need to understand the trajectory of biomarker changes in presymptomatic familial Alzheimer's disease, in order to both assess disease progression and look for therapeutic effects.

The cross-sectional results of the large international Dominantly Inherited Alzheimer Network (DIAN) study have recently been published, indicating that CSF biomarker changes are evident over two decades before an individual's expected age at symptom onset, as determined by their parental age at onset (Bateman *et al.*, 2012). Reduced concentrations of CSF amyloid-β_{42} and increased concentrations of CSF tau were detected at 25 and 15 years from expected symptom onset, respectively. Amyloid-β deposition on Pittsburgh compound B-PET scans (Klunk *et al.*, 2004) and hippocampal volume loss were apparent at 15 years and cerebral hypometabolism at 10 years before expected symptom onset. In the *PSEN1* E280A Colombian kindred, altered hippocampal activation on functional MRI during memory encoding has been observed approximately two decades before expected age at onset (Reiman *et al.*, 2012). Presymptomatic hippocampal atrophy has also been detected in longitudinal studies, which have followed smaller cohorts through the presymptomatic stage to age at symptom onset. At a group level, mutation carriers showed hippocampal and whole brain volume loss compared with control

subjects at 3 and 1 year before symptom onset (Ridha *et al.*, 2006). However, longitudinal measures were able to detect changes earlier, with differences in hippocampal and whole brain atrophy rates observed at 5.5 and 3.5 years before symptom onset in mutation carriers and cortical thinning at 4.1 and 1.8 years presymptomatically for precuneus and posterior cingulate cortex, respectively (Ridha *et al.*, 2006; Knight *et al.*, 2011a).

Previous volumetric imaging studies have mainly focused on the neocortex and hippocampus, in view of the well recognized roles that these structures play in higher cognitive functions and memory, and their apparent vulnerability to Alzheimer's disease pathology. However, Pittsburgh compound B-PET studies have indicated that prominent amyloid deposition first appears in the striatum and thalamus in presymptomatic familial Alzheimer's disease (Klunk *et al.*, 2007; Knight *et al.*, 2011b). These subcortical structures have received relatively little attention from volumetric imaging studies in Alzheimer's disease. They are known to be significantly atrophied in sporadic Alzheimer's disease but it is not known how early this atrophy occurs (de Jong *et al.*, 2008). A recent familial Alzheimer's disease study reported decreased volumes of thalamus, caudate and putamen in presymptomatic mutation carriers who were on average 15 years younger than their family's median age at dementia diagnosis, with a trend towards increasing caudate size in those with memory deficits who were 10 years younger (Lee *et al.*, 2013). Increased caudate volumes were reported in another cohort of presymptomatic mutation carriers who were approximately a decade younger than their expected age at symptom onset (Fortea *et al.*, 2010). This study also included diffusion imaging and found associated changes in mean diffusivity in the caudate of presymptomatic mutation carriers.

Although the thalamus and striatum are structures that are not conventionally associated with Alzheimer's disease, it has long been known that they are affected by Alzheimer's disease pathology (Braak and Braak, 1990, 1991). It is also becoming increasingly recognized that, given their dense connections with the cortex, they are involved in a variety of neural networks subserving complex cognitive and behavioural functions (Middleton and Strick, 2000). The caudate, for example, appears to play a key role in supporting the planning and execution of behaviour needed to achieve complex goals (Grahn *et al.*, 2008), whilst thalamic nuclei are involved in declarative memory function at a number of different levels (Van der Werf *et al.*, 2003). There is a growing appreciation of the idea that Alzheimer's disease, and indeed neurodegenerative diseases in general, should be considered as

network disorders in which there is selective degeneration of vulnerable neuronal circuits (Warren et al., 2012). It therefore seems appropriate to investigate the subcortical grey matter regions involved in such networks, as well as the cortical areas and their connecting white matter.

Diffusion tensor imaging (DTI) allows assessment of alterations in tissue microstructure in specific brain regions and can be used to examine the integrity of connecting white matter pathways (Basser et al., 1994). DTI exploits the fact that water molecules show preferential diffusion along the major axis of a white matter fibre bundle (anisotropy), owing to barriers hindering perpendicular diffusion including axonal membranes and the myelin sheath. The effects of a pathological process on white matter tracts can be explored by investigating whether there are associated changes in the overall magnitude of diffusion (mean diffusivity) or the degree of its directionality (fractional anisotropy). Examining the component eigenvalues of the diffusion tensor, from which fractional anisotropy is derived, provides further information on how diffusion is altered in both the principal direction of the tract (axial diffusivity) and in the plane perpendicular to this (radial diffusivity). If there are changes in axial diffusivity and radial diffusivity which are proportional, there will be no corresponding change in fractional anisotropy, making it important to examine these components separately (Acosta-Cabronero et al., 2010). DTI can be used to characterize grey matter microstructure too (Bozzali et al., 2002; McKinstry et al., 2002), with mean diffusivity a commonly used metric (Benedetti et al., 2006). In fibre-rich structures such as the thalamus and striatum, fractional anisotropy may also be a useful indicator of pathological change (Ciccarelli et al., 2001; Tovar-Moll et al., 2009; Bohanna et al., 2011). Many DTI studies of sporadic Alzheimer's disease have now been published, reporting decreased fractional anisotropy and increased mean diffusivity in various tracts, most notably the cingulum, corpus callosum and white matter of the parahippocampal gyrus (Chua et al., 2008; Stebbins and Murphy, 2009). There has been just one previous DTI study of presymptomatic familial Alzheimer's disease, which examined fractional anisotropy only and found it to be globally reduced in the white matter of presymptomatic mutation carriers, most strikingly in the fornix (Ringman et al., 2007).

We investigated a cohort of PSEN1 presymptomatic mutation carriers who were relatively close to their expected age at symptom onset, together with groups of symptomatic mutation carriers and control subjects. We used region of interest analyses to examine volumetric and diffusivity differences in the subcortical structures that are the main focus of this study, and altered diffusivity in white matter tracts of interest. We also used automated whole brain analysis techniques; voxel-based morphometry and tract-based spatial statistics (TBSS), to provide whole-brain assessments of group differences in volume and DTI indices, respectively.

Materials and methods

Subjects

Twenty PSEN1 muation carriers were included in this study, all of whom had pathogenic mutations that have previously been reported

elsewhere. Ten of these were presymptomatic mutation carriers; three M146I, two E184D and one each of M139V, Y115C, intron 4, L171P, L262F. Ten were symptomatic mutation carriers; three intron 4, two E280G and one each of Y115H, E120K, P264L, R269H and R278I. A group of 20 healthy control subjects (including two gene-negative siblings) was also studied. All subjects in the study underwent assessment with the Mini-Mental State Examination. The PSEN1 mutation carriers also underwent neurological examination and detailed neuropsychological assessment. The neuropsychological test battery comprised measures of general intellectual functioning (Wechsler Abbreviated Scale of Intelligence), estimated premorbid IQ (National Adult Reading Test); verbal and visual recognition memory (Recognition Memory Test for words and faces); naming (Graded Naming Test); calculation (Graded Difficulty Arithmetic Test); visuoperceptual skills (object decision test from the Visual Object and Space Perception battery); speed and executive function (Stroop Test). All mutation carriers identified a close informant who was interviewed separately to gain a collateral history; specific enquiry was made regarding cognitive symptoms in each domain, anxiety and depression. Mutation carriers were defined as symptomatic if consistent symptoms of cognitive decline were reported by the subject and/or their close informant. If there was a discrepancy between the opinion of the subject and their informant, the perspective of the informant was favoured as insight may not always be preserved in familial Alzheimer's disease. Estimated time to onset was calculated for the presymptomatic mutation carriers by subtracting the participant's current age from the age at which their parent first developed symptoms of progressive cognitive decline. The participants were recruited from an ongoing longitudinal study of familial Alzheimer's disease at the Dementia Research Centre, University College London (UCL) Institute of Neurology, which receives research referrals from across the UK. Some of the subjects had participated in our previous imaging studies of familial Alzheimer's disease (Ridha et al., 2006; Knight et al., 2011a, b) but the data used for this study have not been reported elsewhere. All of the subjects in this study were aware of their mutation status, having undergone clinical diagnostic or predictive genetic testing at approved clinical centres separately to their involvement in research. All subjects gave written informed consent according to the Declaration of Helsinki and approval was received from the local ethics committee. Consent was taken by a clinician experienced in the assessment of patients with cognitive impairment and all subjects were considered to have capacity to consent according to the Mental Capacity Act of 2005. Subject demographics are detailed in Table 1.

Magnetic resonance image acquisition

All subjects were scanned on the same 3 T Siemens TIM Trio scanner using a 32-channel phased array head-coil. A sagittal 3D MP-RAGE T_1-weighted volumetric MRI (echo time/repetition time/inversion time = 2.9/2200/900 ms, dimensions of $256 \times 256 \times 208$, voxel size of $1.1 \times 1.1 \times 1.1$ mm) and a coronal T_2 FLAIR sequence (echo time/repetition time/inversion time = 87/9000/2500 ms, voxel size of $0.9375 \times 0.9375 \times 5$ mm) were acquired. Two 64-direction DTI sequences were acquired with a single shot, spin-echo echo planar imaging (EPI) sequence (field of view 240 mm; matrix 96×96; yielding an isotropic voxel size of $2.5 \times 2.5 \times 2.5$ mm; 55 contiguous axial slices; repetition time: 6800 ms; echo time: 91 ms; b-value: 1000 s/mm^2), augmented with parallel imaging acceleration (GRAPPA). Nine acquisitions without diffusion weighting were acquired (b = 0 s/mm^2). For all subjects, volumetric T_1, DTI and T_2 FLAIR images were assessed visually in all planes to ensure adequate coverage and to exclude significant motion, artefacts or unexpected pathology.

Table 1 Subject demographics, neuropsychological and clinical data

	Presymptomatic mutation carriers (4 males, 6 females)	Symptomatic mutation carriers* (6 males, 4 females)	Control subjects (9 males, 11 females)	P-value
Age, years	37.8 (4.7)	49 (9.4)	44.3 (12.7)	0.27[a] (SMC versus control) 0.04[a] (PMC versus control) <0.01[a] (PMC versus SMC)
Years from estimated age at onset	5.6 (7)	N/A	N/A	
Disease duration, years	N/A	4.3 (1.7)	N/A	
MMSE/ 30 (range)	29 (28–30)	19 (13–24)	29.9 (29–30)	<0.01[b] (SMC versus control) 0.02[b] (PMC versus control) <0.01[b] (PMC versus SMC)
Years of education	13 (2.5)	12 (1.7)	N/A	0.20[a]
Neuropsychology				
NART estimated IQ	100.2 (12.9)	100.1 (12.5)	N/A	0.98[a]
WASI Verbal IQ	101.7 (18.0)	81.2 (17.5)	N/A	0.02[a]
WASI Performance IQ	106.7 (17.1)	69.0 (15.0)	N/A	<0.01[a]
RMT words (/50)	45.9 (3.5)	30.0 (8.1)	N/A	<0.01[c]
RMT faces (/50)	42.6 (5.3)	32.4 (7.5)	N/A	<0.01[c]
Graded naming test (/30)	19.0 (5.0)	13.1 (7.8)	N/A	0.5[c]
Graded difficulty arithmetic (/24)	12.9 (6.4)	2.4 (2.4)	N/A	<0.01[c]
Object decision (/20)	18.2 (2.1)	15.6 (3.2)	N/A	0.06[c]
Stroop colour (s)	36.2 (14.8)	63.3 (18.3)	N/A	<0.0[a]
Stroop word (s)	23.1 (8.4)	49.1 (22.1)	N/A	<0.01[a]
Stroop ink colour (s)	58.7 (20.5)	124.4 (30.9)	N/A	<0.01[a]
CLINICAL**				
Anxiety	10%	40%	N/A	
Depression	20%	60%	N/A	
Seizures	0%	0%	N/A	
Myoclonus	40%	60%	N/A	
Pyramidal signs	0%	60%	N/A	
Extrapyramidal signs	0%	20%	N/A	

Values are mean (SD); MMSE = Mini-Mental State Examination; RMT = Recognition Memory Test.

*n = 9 for all neuropsychological measures except Wechsler Abbreviated Scale of Intelligence Performance IQ (WASI PIQ; n = 10), National Adult Reading Test (NART; n = 7) and Stroop colour ink interference (n = 5), with all reductions in n reflecting participants being untestable on specific tasks. Data for the complete cohort were available for all other statistical tests.

**Percentage in group manifesting the clinical feature.

[a] Unpaired t-test, two-tailed test.

[b] Wilcoxon ranksum test.

[c] Linear regression with group and age as independent variables.

Grey matter region of interest volumetric analysis

Region of interest segmentation in T_1-weighted space was used to investigate the volumes of the subcortical structures of interest in this study; namely the thalamus, caudate, putamen and hippocampus. The Multi-Atlas Propagation and Segmentation technique was used (Keihaninejad et al., 2011), which was previously developed for hippocampal segmentation and has been used in brain extraction (Leung et al., 2010, 2011). In Multi-Atlas Propagation and Segmentation, all of the atlases in a template library are first compared with the target image. Our template library consisted of 30 subjects (median age of 31 ± 8 years, 15 females) whose MRI scans had been manually segmented into 83 anatomical structures (Hammers et al., 2003). Multiple best-matched atlases were then selected, and the labels in the selected atlases were propagated to the target image after non-linear image registration. Label fusion was then applied to combine the labels from different atlases to create a consensus segmentation in the target image. We applied Multi-Atlas Propagation and Segmentation to

30 atlas images in a leave-one-out approach in order to determine the number of best-matched atlases (7-9) and the optimal label fusion technique [simultaneous truth and performance level estimation (STAPLE)] (Warfield et al., 2004) required to produce accurate individual regions of interest by comparing them to the manually delineated regions. We used the optimized Multi-Atlas Propagation and Segmentation technique to generate individual regions of interest for each subject in our data set (Fig. 1). The anatomical validity of the segmentations was confirmed by two consultant neuroradiologists.

Grey matter region of interest diffusion tensor imaging analysis

All DTI were registered to the first b = 0 image using 12 degrees of freedom FLIRT (FMRIB Software Library) (Jenkinson et al., 2002) for motion and eddy current correction and realigning diffusion-weighting directions appropriately. Tensor fitting was performed using Camino (Cook et al., 2006). For each subject, the T_1-weighted image was registered to the first (b = 0) DTI image using a 12-parameter affine registration
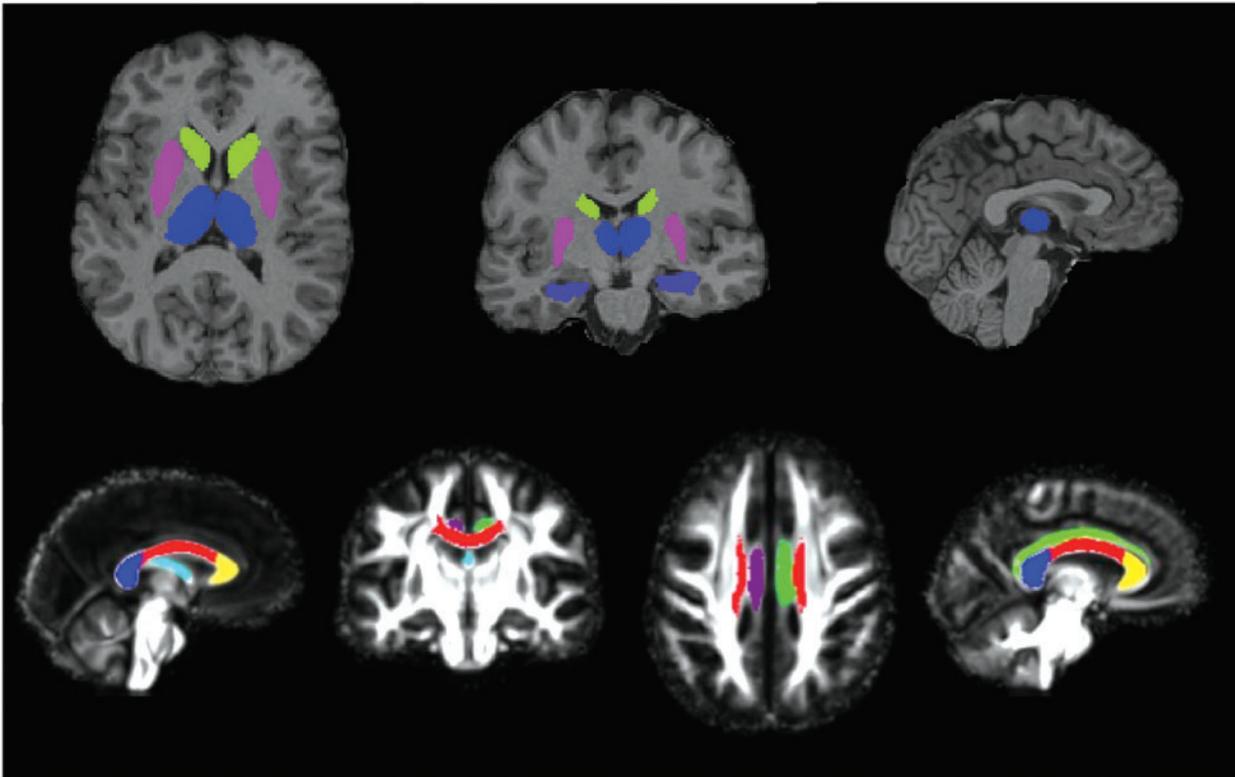
Figure 1 Regions of interest. Grey matter regions of interest (*top*): segmentations of thalamus (blue), caudate (green), putamen (pink) and hippocampus (purple) overlaid on the T_1 image of a single subject. White matter tracts of interest (*bottom*): segmentations of the fornix (pale blue), right cingulum (purple), left cingulum (green), genu (yellow), body (red) and splenium (dark blue) of the corpus callosum, overlaid on the study-specific template.

algorithm (Ourselin *et al.*, 2001). The regions of interest defined using Multi-Atlas Propagation and Segmentation were transferred to the DTI space using nearest-neighbour interpolation. The overall average fractional anisotropy and mean diffusivity values were calculated by averaging values for the entire individual region of interest.

## White matter tract of interest diffusion tensor imaging analysis

White matter tract of interest analysis was performed using DTI-TK to create a study-specific template using iterative tensor-based registration, which takes into account local fibre orientation (Zhang *et al.*, 2006; Keihaninejad *et al.*, 2012a). In particular, all linear and non-linear registrations on the tensor images were performed using DTI-TK, which has recently been shown to outperform the more conventional tools (Wang *et al.*, 2011). Fractional anisotropy, mean, axial and radial diffusivity maps were created for the study-specific template and registered images. The ICBM-DTI-81 white matter labels and tracts atlas, developed by Johns Hopkins University was used to locate the white matter tracts of interest (Mori *et al.*, 2005). The fractional anisotropy map of the Johns Hopkins University atlas was linearly and non-linearly registered to the study-specific template fractional anisotropy map (Ourselin *et al.*, 2001; Modat *et al.*, 2010). This transformation was used to warp the labels from the white matter atlas to the template fractional anisotropy image through nearest neighbour interpolation. In this study, we focused on six white matter tracts of interest: the genu, body, and splenium of the corpus callosum, fornix and left and right cingulum (Fig. 1).

Statistical tests for non-voxelwise analyses

Baseline characteristics and neuropsychological test results (which were converted to z scores, based on published normative data) were compared using *t*-tests for normally distributed variables and Wilcoxon rank sum testing for the Mini-Mental State Examination. Linear regression was used to factor out age effects on neuropsychological tests where no detailed age corrections were available (Recognition Memory Test, Graded Naming Test, Graded Difficulty Arithmetic and Object Decision). For the region of interest analyses, groups were compared using separate linear regressions for each outcome measure, in each region of interest. The region of interest volumetric analyses were adjusted for age, gender and total intracranial volume. The region of interest DTI analyses for grey and white matter were adjusted for age and gender. Total intracranial volume correction is not required for DTI as it assesses microstructural properties that are not expected to be associated with macroscopic head size. All results are reported as statistically significant if $P < 0.05$.

Voxel-based morphometry analysis of volumetric imaging

Voxel-based morphometry processing was carried out using SPM8 (Statistical Parametric Mapping, version 8; Wellcome Trust Centre for Neuroimaging, London, UK). The T_1-weighted scans were segmented into grey and white matter using the new segment toolbox
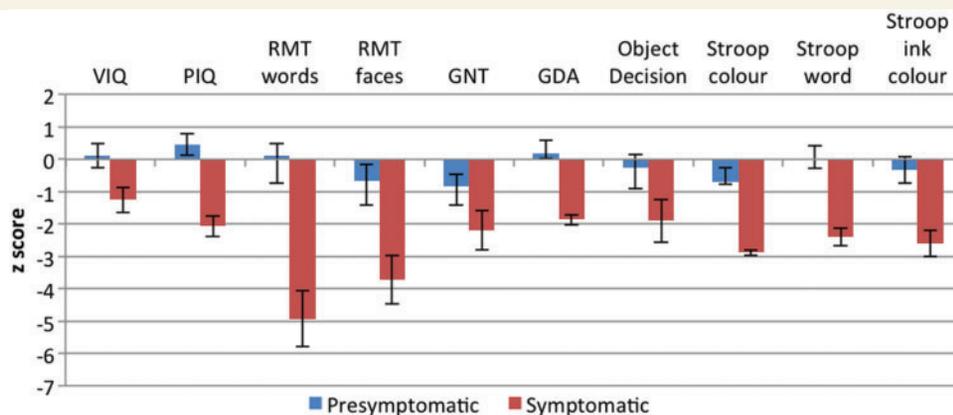
Figure 2 Mean and standard error z-scores for presymptomatic and symptomatic mutation carriers on standard neuropsychological tests. GDA = Graded Difficulty Arithmetic; GNT = Graded Naming Test; PIQ = performance IQ; RMT = Recognition Memory Test; VIQ = verbal IQ.

with default settings (Weiskopf *et al.*, 2011). Segmentations were produced with rigid alignment to standard space [Montreal Neurological Institute (MNI) space] and resampled to 1.5 mm isotropic voxels for use with DARTEL (Ashburner, 2007). DARTEL then iteratively registered the grey and white matter segments to an evolving estimate of their group-wise average (Ashburner and Friston, 2009). The native space tissue segments were then normalized to MNI space using the DARTEL transformations, modulated to account for volume changes. A smoothing kernel of 6 mm full-width at half-maximum was applied. Total intracranial volume was calculated for each subject using Jacobian integration of deformation fields created by the new segment toolbox (Ridgway *et al.*, 2011). Voxel-wise statistical analysis was performed with non-parametric permutation-testing using the FMRIB Software Library randomize program (as used for the TBSS statistical analysis, described below). Grey and white matter images were modelled separately in terms of group (control, presymptomatic, symptomatic), age, gender and total intracranial volume (all mean centred). Statistical significance of differences between groups was assessed using threshold-free cluster enhancement (Smith and Nichols, 2009), controlling family-wise error (FWE). Results for symptomatic patients are shown thresholded at FWE $P < 0.05$; presymptomatic differences are shown at a less stringent level of FWE $P < 0.1$, with effect-maps (difference between adjusted group means as a percentage of the control mean) provided for a fuller characterization of the atrophy pattern.

Voxel-wise diffusion tensor imaging analysis using tract-based spatial statistics

The DTI data were also analysed with TBSS to investigate whole-brain white matter microstructural abnormalities (Smith *et al.*, 2006). In this study the modified TBSS protocol was used by incorporating a group-wise atlas as the registration target; group-wise TBSS (Keihaninejad *et al.*, 2012*b*). In the group-wise TBSS pipeline, a group-wise atlas is first created based on the subset subjects' fractional anisotropy images using the method described in Keihaninejad *et al.* (2012*b*). The voxel-wise statistical analysis was performed by the FSL randomize program (5000 random permutations) with correction for multiple comparisons to control FWE ($P < 0.05$) using threshold-free

cluster enhancement. Age and gender were entered into the analysis as covariates.

Results

The subjects' demographic, neuropsychological and clinical data are summarized in Table 1. The presymptomatic mutation carrier (PMC) group was, as expected, younger than the symptomatic mutation carrier (SMC) group and was on average 5.6 years below the expected age at symptom onset. The mean age of the control group (44.3 years) fell between that of the PMC (37.8 years) and SMC groups (49.0 years) and age was used as a covariate in all analyses, as was gender. There was no clinically relevant difference in Mini-Mental State Examination score between the control subjects and presymptomatic mutation carriers; symptomatic mutation carriers had significantly lower Mini-Mental State Examination scores than both groups as expected.

The PMC and SMC groups were well matched for educational level and estimated premorbid IQ. Figure 2 shows mean and standard error z-scores for the PMC and SMC groups on neuropsychological tests. The PMC group showed no significant deficit on any neuropsychological measure. The SMC group had significantly poorer performance than the PMC group on all tests except naming (Graded Naming Test) and object perception.

The clinical data showed that neuropsychiatric symptoms were common in the SMC group; 40% had anxiety and 60% had depression. In the PMC group, 10% had anxiety and 20% had depression. The two presymptomatic mutation carriers with symptoms of anxiety and/or depression were both within 2 years of their expected age at onset; both had a long history of recurrent psychiatric symptoms since their teenage years and required psychiatric review and medication changes at the time of their current assessment. None of the subjects had seizures but 60% of the symptomatic mutation carriers and 40% of the presymptomatic mutation carriers had myoclonus on neurological examination. Myoclonus was the only abnormal sign present on examination of the presymptomatic mutation carriers but 20% of the symptomatic mutation carriers had extrapyramidal signs and

60% had pyramidal signs, typically a symmetrical spastic increase in lower limb tone with hyper-reflexia.

The grey matter region of interest volumetric analysis demonstrated significant atrophy of the left thalamus in presymptomatic mutation carriers compared with control subjects ($P = 0.023$), together with significant atrophy of both left caudate ($P = 0.025$) and right caudate ($P = 0.001$). Refer to Table 2 for all the grey matter region of interest volumetric and DTI results. No areas of significant grey or white matter volume loss were seen in the PMC group versus control subjects in the less sensitive voxel-based morphometry analysis after correction for multiple comparisons at the conventional level of FWE $P < 0.05$. However, atrophy in the bilateral thalamic region was near significant [FWE $P = 0.061$, at MNI coordinates of (4.5, −13.5, 12) mm]. Results thresholded at FWE $P < 0.1$, together with an unthresholded effect map are shown in Fig. 3. All of the grey matter regions of interest were significantly atrophied in the SMC group compared with control subjects. The voxel-based morphometry results for the SMC versus control group comparison demonstrated grey matter volume loss in bilateral hippocampus and posterior cortical areas but the most significant volume loss was seen in the region of bilateral striatum and thalamus. Extensive loss of white matter volume was also observed in the symptomatic mutation carriers compared with control subjects (Fig. 4).

In the presymptomatic group, no significant hippocampal atrophy was evident, although the right hippocampus did show significantly decreased mean diffusivity ($P = 0.046$) in the grey matter region of interest DTI analysis relative to control subjects. Although not reaching significance, there was also a trend towards decreased mean diffusivity in all the other subcortical structures in presymptomatic mutation carriers. This contrasts with the findings in the symptomatic mutation carriers, who demonstrated increased mean diffusivity in all the subcortical grey matter structures assessed; the pattern of change in diffusivity that is more typically observed in neurodegenerative disease. In the presymptomatic mutation carriers, fractional anisotropy was increased in the left thalamus ($P = 0.016$), right thalamus ($P = 0.036$) and left caudate ($P = 0.004$). Fractional anisotropy was also increased in symptomatic mutation carriers in left putamen ($P = 0.032$) and right putamen ($P = 0.020$), but did not differ significantly from control subjects in the other grey matter structures assessed.

In the white matter tract of interest analysis, presymptomatic mutation carriers demonstrated decreased mean diffusivity ($P = 0.043$) and axial diffusivity ($P = 0.011$) in the right cingulum only (Table 3). Significantly decreased fractional anisotropy with increased mean, axial and radial diffusivity was seen in all the white matter tracts of interest in the symptomatic mutation carriers. The TBSS analysis demonstrated widespread decreased fractional anisotropy and increased mean, axial and radial diffusivity in the white matter of symptomatic mutation carriers. As demonstrated in Fig. 5, the fall in fractional anisotropy in the fornix and cingulum of the SMC group appeared to be driven by an increase in radial diffusivity; very little difference in axial diffusivity was seen in these structures between the symptomatic mutation carriers and control subjects. No significant differences in any of the DTI indices were seen in the TBSS analysis for presymptomatic mutation carriers versus control subjects.

As a supplementary analysis, region of interest measures for the PMC versus SMC groups were compared. Significantly decreased fractional anisotropy with increased mean, axial and radial diffusivity was found in all white matter regions of interest in symptomatic mutation carriers. All grey matter regions of interest except from the caudates had significantly smaller volumes in symptomatic mutation carriers compared with presymptomatic mutation carriers. Whereas fractional anisotropy did not differ, mean diffusivity was significantly increased in all grey matter regions of interest of symptomatic mutation carriers except right thalamus and left caudate, where the increase was of borderline significance ($P = 0.061$ and $P = 0.075$, respectively).

Discussion

It has been established from Pittsburgh compound B-PET imaging studies that the striatum and thalamus are affected early in the presymptomatic stage of familial Alzheimer's disease by amyloid deposition (Klunk et al., 2007; Knight et al., 2011b). We demonstrated atrophy of the caudate and thalamus in a cohort of presymptomatic mutation carriers who were on average 5.6 years prior to their expected age at onset. Half of these presymptomatic mutation carriers had participated in a previous Pittsburgh compound B-PET study, which found increased thalamic and striatal amyloid deposition compared with control subjects (Knight et al., 2011b). The findings of presymptomatic familial Alzheimer's disease studies will clearly depend on how far from symptom onset the individuals in the study are. A previous study examining the caudate in presymptomatic familial Alzheimer's disease interestingly demonstrated an unexpected increase in the volume of the caudate, precuneus and parietotemporal areas in presymptomatic mutation carriers who were on average 9.9 years from expected age at onset (Fortea et al., 2010). The authors of this paper speculated that reactive neuronal hypertrophy and/or inflammatory processes early in the presymptomatic stage may account for an initial increase in the volume of these structures, which then undergo progressive atrophy as the disease progresses. Although their findings, like ours, need to be replicated in larger longitudinal studies, it is quite possible that pathological processes early in the presymptomatic stage cause dynamic changes in the volume of affected structures, which alter in terms of the direction of change as symptom onset is approached. Their DTI results, like ours, showed a widespread increase in mean diffusivity in symptomatic mutation carriers and a contrasting decrease in mean diffusivity in the presymptomatic mutation carriers.

Increased mean diffusivity and decreased fractional anisotropy are thought to reflect loss of integrity of cellular structures and are commonly observed in neurodegenerative diseases, as was the case with the symptomatic mutation carriers in our study. The presymptomatic mutation carriers, on the other hand, showed significantly decreased mean diffusivity in the right hippocampus and a trend towards decreased mean diffusivity in the other subcortical structures studied. Decreased mean diffusivity may reflect earlier pathological changes in the pathway towards neurodegeneration, such as microglial activation/accumulation and swelling of neurons and glia. In a triple transgenic mouse model of Alzheimer's disease

Table 2 Mean ± SD volumes and diffusivity indices in the grey matter regions of interest

	Control subjects	Presymptomatic mutation carriers	Symptomatic mutation carriers
Volume (mm^3)			
Right thalamus	7792 ± 550	7676 ± 747 *275 (−152, 703)*	6103 ± 543 *1620 (1294, 1947)**
Left thalamus	7177 ± 652	6962 ± 604 *428 (64, 792)**	5520 ± 404 *1533 (1216, 1849)**
Right caudate	4689 ± 512	4273 ± 553 *605 (293, 917)**	3832 ± 525 *746 (438, 1053)**
Left caudate	4743 ± 506	4376 ± 610 *466 (63, 868)**	3748 ± 588 *940 (537, 1343)**
Right putamen	5210 ± 656	5234 ± 695 *144 (−250, 537)*	4228 ± 473 *920 (555, 1285)**
Left putamen	5035 ± 680	4989 ± 775 *194 (−232, 620)*	3847 ± 655 *1142 (736, 1548)**
Right hippocampus	3131 ± 304	3153 ± 483 *−1.76 (−233, 230)*	2295 ± 477 *868 (632, 1103)**
Left hippocampus	3014 ± 278	3118 ± 423 *−116 (−345, 112)*	2302 ± 459 *769 (546, 991)**
Fractional anisotropy			
Right thalamus	0.352 ± 0.017	0.367 ± 0.019 *−0.017 (−0.032, −0.001)**	0.346 ± 0.031 *0.006 (−0.014, 0.025)*
Left thalamus	0.332 ± 0.013	0.343 ± 0.008 *−0.013 (−0.023, −0.003)**	0.327 ± 0.031 *0.007 (−0.011, 0.025)*
Right caudate	0.229 ± 0.024	0.239 ± 0.030 *−0.017 (−0.038, 0.004)*	0.243 ± 0.034 *−0.013 (−0.037, 0.010)*
Left caudate	0.226 ± 0.017	0.248 ± 0.026 *−0.025 (−0.041, −0.009)**	0.236 ± 0.027 *−0.011 (−0.029, 0.008)*
Right putamen	0.222 ± 0.016	0.227 ± 0.013 *−0.009 (−0.021, 0.003)*	0.242 ± 0.020 *−0.017 (−0.031, −0.003)**
Left putamen	0.212 ± 0.011	0.214 ± 0.010 *−0.005 (−0.013, 0.003)*	0.228 ± 0.021 *−0.014 (−0.027, −0.001)**
Right hippocampus	0.184 ± 0.016	0.193 ± 0.022 *−0.006 (−0.0214, 0.009)*	0.176 ± 0.032 *0.004 (−0.014, 0.023)*
Left hippocampus	0.178 ± 0.019	0.192 ± 0.020 *−0.012 (−0.029, 0.005)*	0.167 ± 0.033 *0.007 (−0.013, 0.028)*
Mean diffusivity			
Right thalamus	0.824 ± 0.030	0.794 ± 0.043 *0.022 (−0.006, 0.049)*	0.912 ± 0.089 *−0.075 (−0.119, −0.032)**
Left thalamus	0.838 ± 0.029	0.815 ± 0.037 *0.016 (−0.010, 0.042)*	0.915 ± 0.069 *−0.070 (−0.108, −0.032)**
Right caudate	0.956 ± 0.071	0.949 ± 0.068 *0.005 (−0.057, 0.066)*	1.075 ± 0.111 *−0.113 (−0.185, −0.040)**
Left caudate	0.993 ± 0.081	0.955 ± 0.066 *0.013 (−0.045, 0.071)*	1.058 ± 0.072 *−0.052 (−0.112, 0.008)*
Right putamen	0.761 ± 0.026	0.740 ± 0.028 *0.016 (−0.006, 0.038)*	0.840 ± 0.060 *−0.075 (−0.108, −0.041)**
Left putamen	0.773 ± 0.040	0.752 ± 0.021 *0.012 (−0.016, 0.039)*	0.838 ± 0.061 *−0.061 (−0.010, −0.022)**
Right hippocampus	0.958 ± 0.033	0.907 ± 0.073 *0.044 (0.002, 0.087)**	1.094 ± 0.073 *−0.139 (−0.181, −0.096)**
Left hippocampus	0.952 ± 0.052	0.921 ± 0.053 *0.027 (−0.017, 0.072)*	1.113 ± 0.096 *−0.163 (−0.221, −0.104)**

The differences in adjusted means between the mutation carriers and control group (95% confidence interval) are shown in italics. Significant results at $P < 0.05$ are indicated by an asterisk.

the appearance of neuritic plaques is associated with hippocampal astrogliosis and microglial activation and is preceded by an increase in the density of resting microglia (Olabarria et al., 2010; Rodriguez et al., 2010). A DTI study of the APPsw transgenic mouse found that the time of significant amyloid plaque accumulation coincided with a fall in the magnitude of diffusion in hippocampus and cerebral cortex (Sun et al., 2005). Microglial activation PET studies have demonstrated increased thalamic binding following traumatic brain injury (Ramlackhansingh et al., 2011) and middle cerebral artery infarction (Pappata et al., 2000), with decreased thalamic mean diffusivity seen initially in acute stroke (Herve et al., 2005), perhaps supporting the
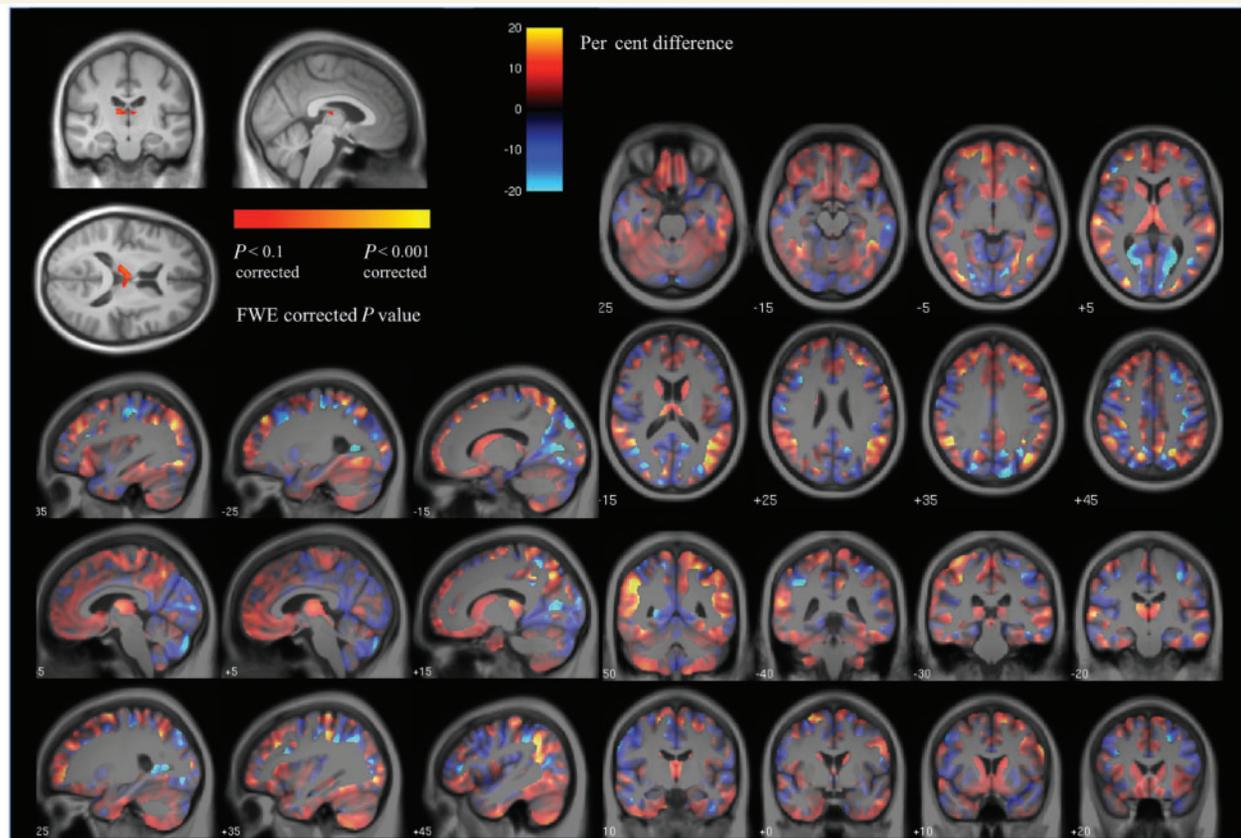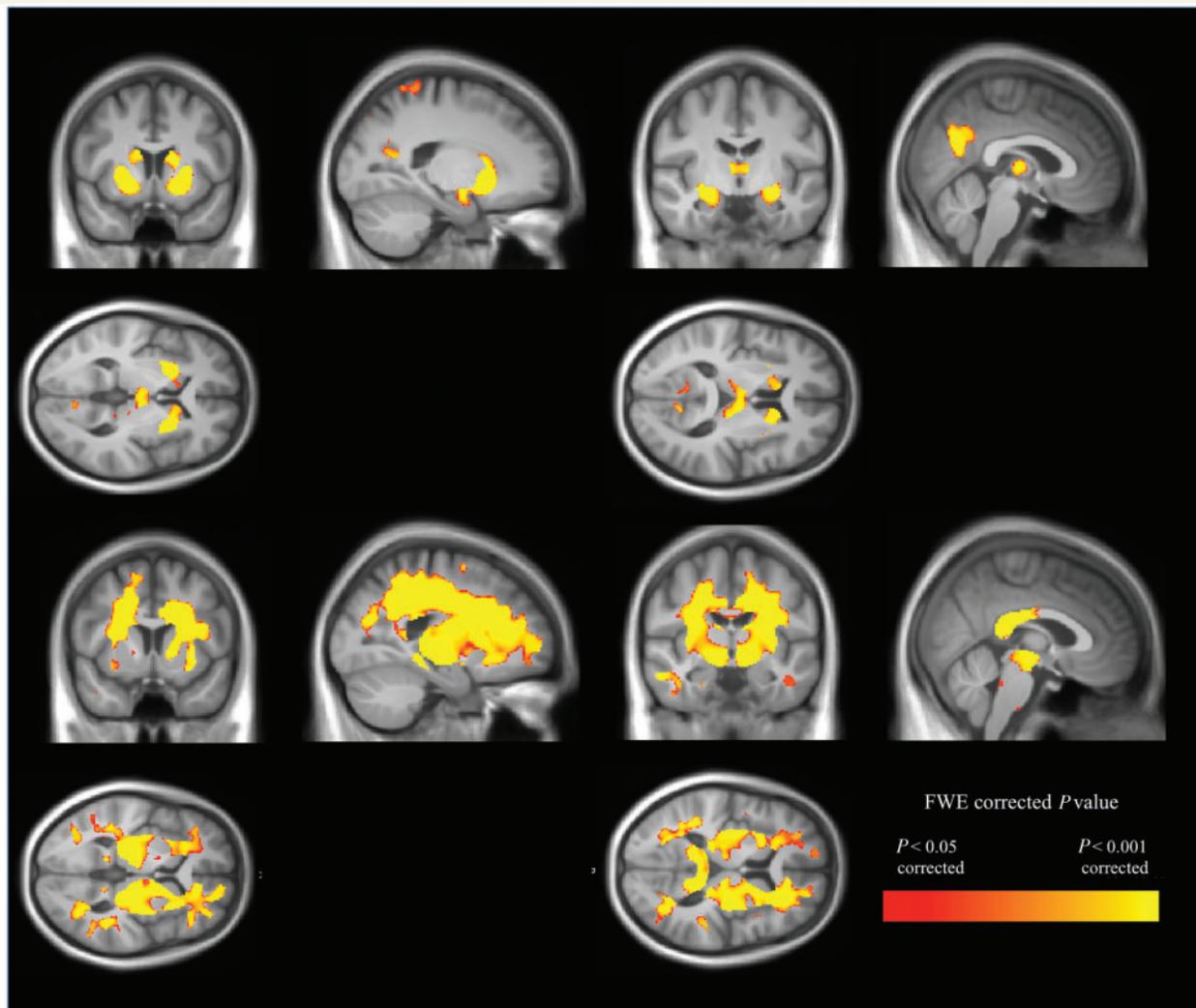
Figure 3 Voxel-based morphometry results showing (*top left*) areas of grey matter reduction in presymptomatic mutation carriers compared with control subjects after correction for multiple comparisons at FWE < 0.1 and the effect-map for the PMC versus control group comparison. In the effect-map, regions showing reduced grey matter in the PMC group are shown in red and in control subjects in blue. Differences between the two adjusted group-means are overlaid on a mean study-specific template. Images shown in radiological convention (right on left).

hypothesis that gliosis accounts for the low mean diffusivity observed in presymptomatic mutation carriers. Microglia undergo persistent activation at sites of white matter damage (Wilson *et al.*, 2004), which may explain why they are observed in densely connected subcortical structures. In axonal injury, APP is upregulated in white matter at the site of trauma but is later seen in the dorsal thalamus (Spain *et al.*, 2010), where neuronal atrophy, but not cell death, has been observed (Lifshitz *et al.*, 2007).

The PMC group in our study showed increased fractional anisotropy in bilateral thalamus and left caudate and, in the SMC group, increased putamen fractional anisotropy was seen bilaterally. Fractional anisotropy reflects the degree of directionality of diffusion of water molecules within a structure; it is therefore highest in white matter tracts, lower in grey matter and lowest in CSF. The anisotropy of the thalamus and striatum is probably due to their compartmentalized cytoarchitectural organization, together with the large number of white matter fibres passing through them (Wiegell *et al.*, 2000). Similar to our findings, a pattern of increased fractional anisotropy in the thalamus and basal ganglia has been observed in patients with multiple sclerosis (Ciccarelli *et al.*, 2001; Tovar-Moll *et al.*, 2009). It has been suggested that this may be due to the selective degeneration of white matter fibres connecting these subcortical structures with cortical areas combined with the relative preservation of anisotropic intrinsic connections between the structures themselves. This may result in an overall increase in the fractional anisotropy of the subcortical structures. By the same presumed mechanism, increased fractional anisotropy was found in a group of patients with mild cognitive impairment compared with control subjects in the centrum semi-ovale, due to degeneration of association fibres of the superior longitudinal fasciculus where they cross with intact motor projection fibres (Douaud *et al.*, 2011).

Decreased mean diffusivity and axial diffusivity were observed in the right cingulum of the PMC group, whereas increased mean, axial and radial diffusivity occurred in all white matter regions of interest of the symptomatic mutation carriers. This pattern of events also conforms with the findings of pathological studies of axonal damage. Axonal injury initially causes swelling, beading and fragmentation of axons with an associated fall in axial diffusivity, probably because intracellular diffusion is hindered by the damaged membranes whilst axonal swelling and beading impedes diffusion in both the intracellular and extracellular space (Budde and Frank, 2010). Following subsequent clearance of membrane fragments, the decreased axonal density permits increased parallel diffusion in the extra-axonal space and therefore increased axial diffusivity, together with increased radial diffusivity

Figure 4 Voxel-based morphometry results showing (*top*) grey matter reduction and (*bottom*) white matter reduction in symptomatic mutation carriers compared with control subjects. Results are shown overlaid on a mean study-specific template and are FWE-corrected for multiple comparisons. Images shown in radiological convention (right on left).

secondary to myelin degradation (Song *et al.*, 2003; Concha *et al.*, 2006). In the APPsw transgenic mouse DTI study, decreased axial diffusivity was seen diffusely in the white matter from the time of amyloid plaque accumulation, with increased radial diffusivity occurring in the corpus callosum at a later stage (Sun *et al.*, 2005). Although each variable was examined separately, the TBSS results in our study suggest a more prominent increase in radial than axial diffusivity in symptomatic mutation carriers compared with control subjects, particularly in the fornix and cingulum, which may be because of this gradual transition of axial diffusivity from decreased to increased with advancing axonal degeneration. Other studies of early Alzheimer's disease have also found more prominent increases in radial than axial diffusivity, with axial diffusivity decreased in some tracts (Huang *et al.*, 2007).

Several pathogenic pathways are likely to contribute to the axonal degeneration witnessed in Alzheimer's disease, including defects in fast axonal transport resulting from enhanced

production of amyloid-β (Kanaan *et al.*, 2013). Neurons, having longer dendrites and axons than any other cell type, are particularly vulnerable to impaired fast axonal transport, which may be why familial Alzheimer's disease-causing mutations selectively affect neurons despite being ubiquitously expressed in cells throughout the body. It may also explain why short interneurons tend to be relatively spared in Alzheimer's disease compared with long projection neurons (Mattson and Magnus, 2006), an observation that could well underlie our finding of increased fractional anisotropy in the thalamus and caudate in presymptomatic familial Alzheimer's disease. The cingulum bundle, where we observed presymptomatic diffusivity changes, is composed of particularly long-coursing white matter tracts, arising from the thalamus, cingulate gyrus and cortical association areas. It is the major route for projections from the anterior thalamus to cingulate cortex, hippocampus and retrohippocampal regions; a network that is thought to play a key role in memory and spatial orientation (Neave *et al.*, 1997). These cognitive functions are often impaired early in

Table 3 Mean ± SD diffusivity indices in the white matter tracts of interest

	Control	Presymptomatic	Symptomatic
Fractional anistropy			
Genu of corpus callosum	0.610 ± 0.026	0.621 ± 0.040 *0.010 (−0.017, 0.037)*	0.570 ± 0.010 *−0.040 (−0.059, −0.021)**
Body of corpus callosum	0.612 ± 0.026	0.613 ± 0.045 *−0.000 (−0.029, 0.028)*	0.559 ± 0.012 *−0.054 (−0.074, −0.034)**
Splenium of corpus callosum	0.684 ± 0.020	0.691 ± 0.028 *0.005 (−0.015, 0.025)*	0.639 ± 0.020 *−0.045 (−0.063, −0.027)**
Fornix	0.426 ± 0.044	0.458 ± 0.094 *0.017 (−0.036, 0.069)*	0.332 ± 0.046 *−0.092 (−0.130, −0.054)**
Right cingulum	0.481 ± 0.033	0.503 ± 0.059 *0.018 (−0.018, 0.054)*	0.402 ± 0.019 *−0.078 (−0.102, −0.054)**
Left cingulum	0.457 ± 0.035	0.467 ± 0.050 *0.011 (−0.023, 0.044)*	0.385 ± 0.018 *−0.073 (−0.098, −0.047)**
Mean diffusivity			
Genu of corpus callosum	0.849 ± 0.043	0.835 ± 0.057 *0.010 (−0.031, 0.052)*	0.942 ± 0.026 *0.090 (0.058, 0.122)**
Body of corpus callosum	0.858 ± 0.039	0.855 ± 0.052 *−0.000(−0.038, 0.037)*	0.966 ± 0.041 *0.105 (0.071, 0.139)**
Splenium of corpus callosum	0.855 ± 0.040	0.847 ± 0.068 *0.002 (−0.042, 0.046)*	0.974 ± 0.068 *0.117 (0.073, 0.160)**
Fornix	1.718 ± 0.199	1.642 ± 0.388 *0.007 (−0.214, 0.229)*	2.107 ± 0.147 *.369 (0.215, 0.523)**
Right cingulum	0.821 ± 0.043	0.776 ± 0.047 *0.040 (0.001, 0.078)**	0.980 ± 0.049 *0.157 (0.119, 0.196)**
Left cingulum	0.776 ± 0.050	0.752 ± 0.062 *0.019 (−0.028, 0.066)*	0.911 ± 0.040 *0.132 (0.092, 0.172)**
Axial diffusivity			
Genu of corpus callosum	1.543 ± 0.038	1.528 ± 0.041 *0.010 (−0.023, 0.044)*	1.636 ± 0.031 *0.088 (0.059, 0.118)**
Body of corpus callosum	1.569 ± 0.040	1.562 ± 0.021 *0.003 (−0.027, 0.033)*	1.661 ± 0.041 *0.087 (0.054, 0.120)**
Splenium of corpus callosum	1.662 ± 0.043	1.653 ± 0.075 *0.004 (−0.044, 0.052)*	1.795 ± 0.078 *0.130 (0.082, 0.178)**
Fornix	2.536 ± 0.188	2.454 ± 0.335 *0.021 (−0.177, 0.219)*	2.832 ± 0.136 *0.279 (0.134, 0.424*)*
Right cingulum	1.291 ± 0.046	1.248 ± 0.020 *0.042 (0.010, 0.074)**	1.394 ± 0.054 *0.102 (0.062, 0.142)**
Left cingulum	1.188 ± 0.049	1.161 ± 0.039 *0.018 (−0.021, 0.057)*	1.281 ± 0.043 *0.088 (0.049, 0.128)**
Radial diffusivity			
Genu of corpus callosum	0.503 ± 0.048	0.488 ± 0.068 *0.010 (−0.037, 0.057)*	0.595 ± 0.026 *0.090 (0.055, 0.125)**
Body of corpus callosum	0.503 ± 0.043	0.502 ± 0.069 *−0.002 (−0.047, 0.043)*	0.618 ± 0.042 *0.114 (0.078, 0.151)**
Splenium of corpus callosum	0.451 ± 0.041	0.444 ± 0.066 *0.001 (−0.042, 0.044)*	0.563 ± 0.064 *0.110 (0.068, 0.152)**
Fornix	1.310 ± 0.206	1.236 ± 0.416 *0.001 (−0.234, 0.235)*	1.744 ± 0.155 *0.415 (0.255, 0.575)**
Right cingulum	0.585 ± 0.050	0.540 ± 0.073 *0.039 (−0.012, 0.089)*	0.772 ± 0.048 *0.185 (0.143, 0.227)**
Left cingulum	0.569 ± 0.057	0.547 ± 0.079 *0.019 (−0.036, 0.075)*	0.725 ± 0.043 *0.154 (0.109, 0.198)**

The differences in adjusted means between the mutation carriers and control group (95% confidence interval) are shown in italics. Significant results at $P < 0.05$ are indicated by an asterisk.

Alzheimer's disease, perhaps because neurons lose their functional connections with increasing axonal damage. Eventually, once the damage has reached a stage where trophic signalling is no longer available, overt neurodegeneration may occur.

A number of strands of evidence suggest that a network of limbic neurons undergoes selective degeneration in early Alzheimer's disease, including PET findings of hypometabolism in the thalamus, mamillary bodies, hippocampus and posterior
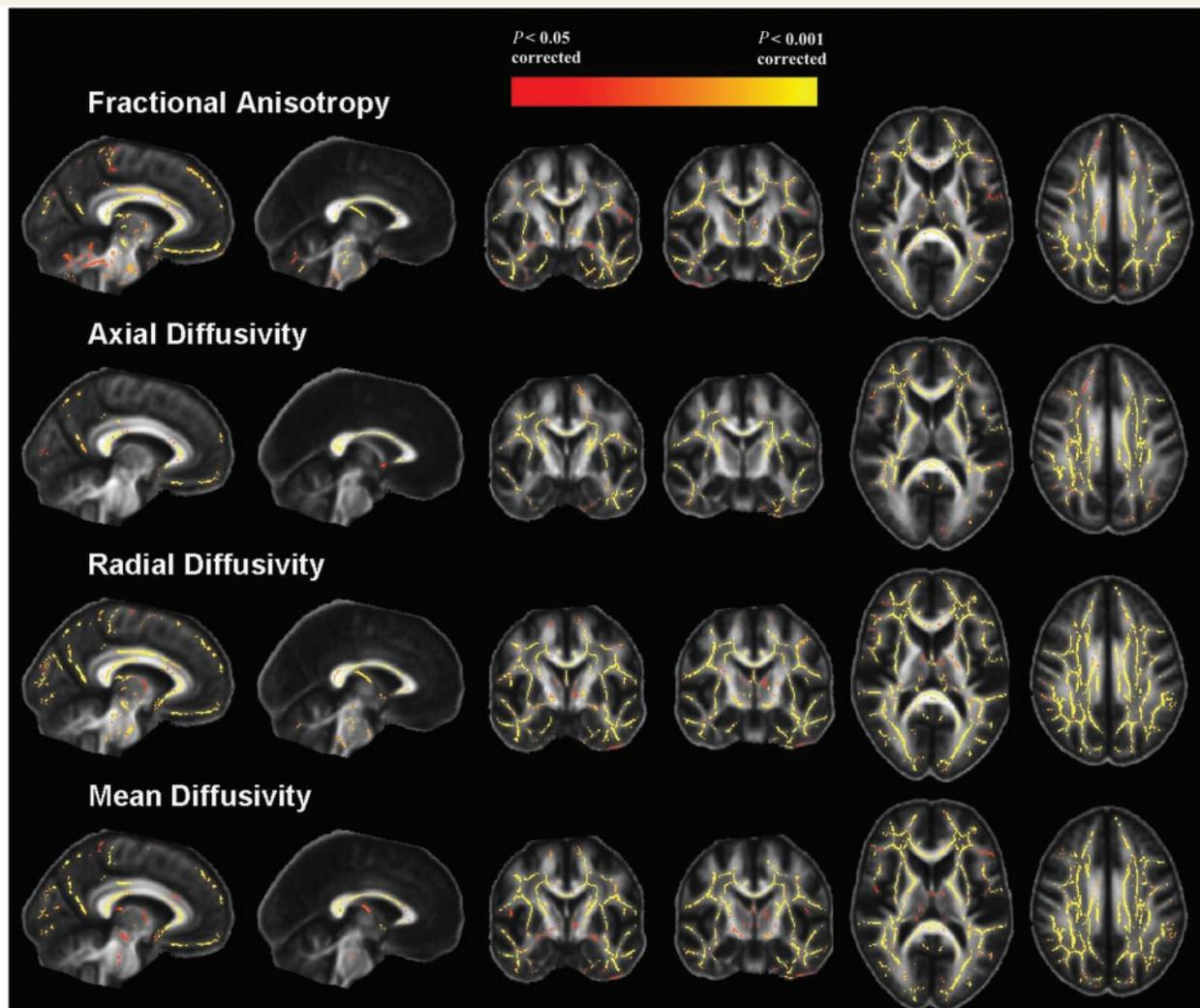
Figure 5 TBSS results demonstrating areas of significantly decreased fractional anisotropy and significantly increased axial, radial and mean diffusivity in symptomatic mutation carriers compared with control subjects. Results are FWE-corrected for multiple comparisons using threshold-free cluster enhancement.

cingulate (Nestor *et al.*, 2003). Along with the cingulum findings, our observation of presymptomatic thalamic atrophy and increased thalamic fractional anisotropy in familial Alzheimer's disease adds further support to this notion. The few pathological studies of thalamic involvement in Alzheimer's disease have demonstrated extracellular amyloid deposits in almost all thalamic nuclei (Braak and Braak, 1991) and significant thalamic atrophy, thought largely to be due to loss of axons, dendrites and synaptic structures or glial cell changes (Xuereb *et al.*, 1991).

The striatum of patients with Alzheimer's disease at post-mortem has also been found to contain abundant amyloid deposits with loss of large cholinergic neurons (Oyanagi *et al.*, 1987; Braak and Braak, 1990), which potentially underlies our findings of striatal atrophy in familial Alzheimer's disease. The majority of striatal nerve cells appear to resist the development of neuritic change (Braak and Braak, 1990) despite the presence of abundant amyloid, which is intriguing given that striatal involvement on Pittsburgh compound B-PET scans is evident over a

decade before symptom onset in familial Alzheimer's disease. One possible hypothesis relates to differences in mechanisms of calcium homeostasis in different neuronal populations. It has been found that presenilins act as calcium leak channels in the endoplasmic reticulum of hippocampal neurons and many *PSEN1* mutations impair this leak function, resulting in endoplasmic reticulum calcium overload and supranormal calcium release. In medium spiny striatal neurons (the major neuronal cell type in the striatum), the endoplasmic reticulum is much less leaky for calcium and presenilins show less involvement in calcium homeostasis (Nelson *et al.*, 2010).

The idea that widespread white matter degeneration occurs in familial Alzheimer's disease is supported by the imaging findings in our SMC cohort. Volume loss of the white matter appeared to be more widespread than that of the grey matter in the voxel-based morphometry analysis, and the TBSS results showed very diffuse microstructural white matter abnormalities in the SMC cohort. A variety of *PSEN1* mutations are known to be associated with

spastic paraparesis and some individuals with the phenotype have white matter hyperintensities visible on brain MRI (O'Riordan et al., 2002; Ryan and Rossor, 2010). It would not, therefore, be surprising if microstructural damage to the white matter gave rise to more subtle pyramidal signs and our observation that 60% of the symptomatic mutation carriers had lower limb spasticity and hyper-reflexia may well relate to this white matter pathology. It is not clear whether there are clinical correlates of the presymptomatic thalamic and caudate changes we observed. Although extrapyramidal signs, often associated with striatal pathology, were seen in 20% of the symptomatic mutation carriers they were not seen presymptomatically. Presymptomatic myoclonus was observed, as has been detected in previous studies (Godbolt et al., 2004). The origin of this myoclonus is unknown but it is possible that thalamocortical networks are implicated, as they are in other conditions such as juvenile myoclonic epilepsy (Gerschlager and Brown, 2009).

Neuropsychologically, the SMC cohort showed deficits in widespread domains at the time they were studied, with verbal recognition memory worst affected and perhaps some relative preservation of naming and object perception, as has been observed previously (Warrington et al., 2001; Godbolt et al., 2004). No significant neuropsychological deficits were observed in the PMC group, although 20% of these subjects and 60% of the symptomatic mutation carriers had symptoms of depression and/or anxiety. Anxiety and depression are relatively common in both sporadic and familial Alzheimer's disease and it is understandable that these symptoms may occur in presymptomatic mutation carriers who are aware of their mutation status and approaching the age at which they saw their parent develop symptoms. However, it is worth noting that limbic circuits are well known to be involved in emotional expression and lesions to anterior thalamic nuclei have been found to cause a variety of neuropsychiatric symptoms including sadness, agitation and flattened affect, in addition to amnesia (Schmahmann, 2003). Disentangling whether presymptomatic psychiatric symptoms are related more to psychological factors or disease effects will require longitudinal study of large cohorts of 'at risk' individuals, comprising both mutation-positive and -negative individuals, who are unaware of their mutation status but exposed to the same anxieties about the possibility of developing symptoms. Collaborative studies such as DIAN will be ideally placed to address these issues and ascertain whether our findings are reproducible in larger familial Alzheimer's disease cohorts.

Our study had several limitations. Subject numbers were relatively small, which limits power and may have accounted for the fact that reduced thalamic volume and increased caudate fractional anisotropy only reached statistical significance on the left in the PMC region of interest analysis. Larger cohorts will be required to investigate whether the onset of subcortical imaging changes is indeed asymmetrical. The optimization of methods for processing and analysing DTI data is an area of active research. One potential issue with DTI is its sensitivity to susceptibility artefacts arising from neighbouring tissues having very different paramagnetic properties, which can lead to distortions of echo planar imaging and misregistration. The lack of echo planar imaging distortion correction in our study should be considered a minor limitation, however the deep grey matter structures of interest in this study do not tend to be severely affected by such artefacts and a gold standard solution to the problem has not yet been established (Gholipour et al., 2011). We used mean fractional anisotropy to investigate the regions of interest, which is common practice in the literature, but is nevertheless an aspect that could be improved in future work. Regional analysis (e.g. of thalamus) cannot easily address subregional variation in the structure of interest. Inspection of the grey matter region of interest histograms indicates a degree of non-normality (distributions are slightly skewed and heavier tailed to the right), which might motivate consideration of robust statistics, such as trimmed-mean or an m-estimator (Hampel et al., 1986). Secondly, and more fundamentally, the nature of fractional anisotropy as a ratio suggests that the use of an arithmetic mean (or robust version thereof) might not be optimal as a measure of central tendency. For example, a geometric mean (corresponding to a logarithmic distance metric) is more appropriate for strictly positive but otherwise unbounded quantities. However, fractional anisotropy is bounded between 0 and 1, and the optimal metric and mean are unclear. More radically, it has been suggested that fractional anisotropy should be replaced with a different measure of anisotropy known as the geodesic anisotropy (Batchelor et al., 2005), which would have a stronger theoretical basis than the combination of fractional anisotropy with robust non-arithmetic averages, but requires further empirical evaluation.

In summary, we demonstrated presymptomatic thalamic and caudate volume loss and increased fractional anisotropy, with altered diffusivity in the right hippocampus and cingulum, in PSEN1 mutation carriers who were ~5.6 years from expected age at onset. We propose that axonal degeneration is an early event in familial Alzheimer's disease pathogenesis and that amyloid accumulation, atrophy and diffusivity changes are seen early on in the thalamus and striatum due to the large number of white matter tracts that these structures are connected with. Involvement of a subcortical structure like the thalamus, which forms a key node in a vulnerable neuronal network, could potentiate the propagation of pathology through that network. The most striking degeneration may then be observed in connected neuronal populations, such as those of the hippocampus. How generalizable our findings are to sporadic Alzheimer's disease is an important question. There is some evidence of early white matter tract degeneration in sporadic Alzheimer's disease from DTI studies of mild cognitive impairment (Chua et al., 2008; Stebbins and Murphy, 2009) and thalamic atrophy has also been demonstrated in mild cognitive impairment (Pedro et al., 2012). In healthy control subjects at increased risk of sporadic Alzheimer's disease due to possession of an apolipoprotein E4 allele, decreased fractional anisotropy has been found in several white matter tracts including the cingulum (Smith et al., 2010) and volume loss of the hippocampus, but not thalamus or striatum, has been observed (O'Dwyer et al., 2012). The same neuronal network appears to disintegrate in both sporadic and familial Alzheimer's disease but it may be that different nodes of this circuit are particularly vulnerable to different risk factors for the disease. The development of more sensitive diffusion imaging techniques such as high-angular-resolution diffusion imaging (HARDI) (Haroon et al., 2011) and

neurite orientation dispersion and density imaging (NODDI) (Zhang *et al.*, 2012), and their application to the longitudinal study of individuals at risk of both familial and sporadic Alzheimer's disease, may allow us to further investigate just how early microstructural abnormalities become evident and when is the optimal time for therapeutic intervention.

References

Acosta-Cabronero J, Williams GB, Pengas G, Nestor PJ. Absolute diffusivities define the landscape of white matter degeneration in Alzheimer's disease. Brain 2010; 133: 529–39.

Ashburner J. A fast diffeomorphic image registration algorithm. Neuroimage 2007; 38: 95–113.

Ashburner J, Friston KJ. Computing average shaped tissue probability templates. Neuroimage 2009; 45: 333–41.

Basser PJ, Mattiello J, LeBihan D. MR diffusion tensor spectroscopy and imaging. Biophys J 1994; 66: 259–67.

Batchelor PG, Moakher M, Atkinson D, Calamante F, Connelly A. A rigorous framework for diffusion tensor calculus. Magn Reson Med 2005; 53: 221–5.

Bateman RJ, Aisen PS, De Strooper B, Fox NC, Lemere CA, Ringman JM, et al. Autosomal-dominant Alzheimer's disease: a review and proposal for the prevention of Alzheimer's disease. Alzheimers Res Ther 2011; 3: 1.

Bateman RJ, Xiong C, Benzinger TL, Fagan AM, Goate A, Fox NC, et al. Clinical and biomarker changes in dominantly Inherited Alzheimer's disease. N Engl J Med 2012; 367: 795–804.

Benedetti B, Charil A, Rovaris M, Judica E, Valsasina P, Sormani MP, et al. Influence of aging on brain gray and white matter changes assessed by conventional, MT, and DT MRI. Neurology 2006; 66: 535–9.

Bohanna I, Georgiou-Karastianis N, Egan GF. Connectivity-based segmentation of the striatum in Huntinton's disease: vulnerability of motor pathways. Neurobiol Dis 2011; 42: 475–81.

Bozzali M, Cercignani M, Sormani MP, Comi G, Filippi M. Quantification of brain gray matter damage in different MS phenotypes by use of diffusion tensor MR imaging. AJNR Am J Neuroradiol 2002; 23: 985–8.

Braak H, Braak E. Alzheimer's disease: striatal amyloid deposits and neurofibrillary changes. J Neuropathol Exp Neurol 1990; 49: 215–24.

Braak H, Braak E. Alzheimer's disease affects limbic nuclei of the thalamus. Acta Neuropathol 1991; 81: 261–8.

Budde MD, Frank JA. Neurite beading is sufficient to decrease the apparent diffusion coefficient after ischemic stroke. Proc Natl Acad Sci USA 2010; 107: 14472–7.

Chua TC, Wen W, Slavin MJ, Sachdev PS. Diffusion tensor imaging in mild cognitive impairment and Alzheimer's disease: a review. Curr Opin Neurol 2008; 21: 83–92.

Ciccarelli O, Werring DJ, Wheeler-Kingshott CA, Barker GJ, Parker GJ, Thompson AJ, et al. Investigation of MS normal-appearing brain using diffusion tensor MRI with clinical correlations. Neurology 2001; 56: 926–33.

Cook PA, Bai Y, Nedjati-Gilani S, Seunarine KK, Hall MG, Parker GJ, et al. Camino: open-source diffusion-MRI reconstruction and processing [abstract]. Proc Int Soc Mag Reson Med 2006; 14.

Concha L, Gross DW, Wheatley BM, Beaulieu C. Diffusion tensor imaging of time-dependent axonal and myelin degradation after corpus callosotomy in epilepsy patients. Neuroimage 2006; 32: 1090–9.

de Jong LW, van der Hiele K, Veer IM, Houwing JJ, Westendorp RG, Bollen EL, et al. Strongly reduced volumes of putamen and thalamus in Alzheimer's disease: an MRI study. Brain 2008; 131: 3277–85.

Douaud G, Jbabdi S, Behrens TE, Menke RA, Gass A, Monsch A, et al. DTI measures in crossing-fibre areas: increased diffusion anisotropy reveals early white matter alteration in MCI and mild Alzheimer's disease. Neuroimage 2011; 55: 880–90.

Ferri CP, Prince M, Brayne C, Brodaty H, Fratiglioni L, Ganguli M, et al. Global prevalence of dementia: a Delphi consensus study. Lancet 2005; 366: 2112–17.

Fortea J, Sala-Llonch R, Bartres-Faz D, Bosch B, Lladó A, Bargalló N, et al. Increased cortical thickness and caudate volume precede atrophy in PSEN1 mutation carriers. J Alzheimers Dis 2010; 22: 909–22.

Gerschlager W, Brown P. Myoclonus. Curr Opin Neurol 2009; 22: 414–18.

Gholipour A, Kehtarnavaz N, Scherrer B, Warfield S. On the accuracy of unwarping techniques for the correction of susceptibility-induced geometric distortion in magnetic resonance echo-planar images [abstract]. Conf Proc IEEE Eng Med Biol Soc 2011; 2011: 6997–7000.

Godbolt AK, Cipolotti L, Watt H, Fox NC, Janssen JC, Rossor MN. The natural history of Alzheimer disease: a longitudinal presymptomatic and symptomatic study of a familial cohort. Arch Neurol 2004; 61: 1743–8.

Grahn JA, Parkinson JA, Owen AM. The cognitive functions of the caudate nucleus. Prog Neurobiol 2008; 86: 141–55.

Hammers A, Allom R, Koepp MJ, Free SL, Myers R, Lemieux L, et al. Three-dimensional maximum probability atlas of the human brain, with particular reference to the temporal lobe. Hum Brain Mapp 2003; 19: 224–47.

Hampel FR, Ronchetti EM, Rousseeuw PJ, Stahel WA. Robust statistics: The approach based on influence functions. New York: Wiley; 1986.

Haroon HA, Reynolds H, Carter SF, Embleton KV, Herholz KG, Parker GJ. HARDI-based microstructural complexity mapping reveals distinct subcortical and cortical grey matter changes in mild cognitive

impairment and Alzheimer's disease [abstract]. Proc Int Soc Mag Reson Med 2011; 682.

Herve D, Molko N, Pappata S, Buffon F, LeBihan D, Bousser M, et al. Longitudinal thalamic diffusion changes after middle cerebral artery infarcts. J Neurol Neurosurg Psychiatry 2005; 76: 200–5.

Huang J, Friedland RP, Auchus AP. Diffusion tensor imaging of normal-appearing white matter in mild cognitive impairment and early Alzheimer disease: preliminary evidence of axonal degeneration in the temporal lobe. AJNR Am J Neuroradiol 2007; 28: 1943–8.

Jenkinson M, Bannister P, Brady M, Smith S. Improved optimization for the robust and accurate linear registration and motion correction of brain images. Neuroimage 2002; 17: 825–41.

Kanaan NM, Pigino GF, Brady ST, Lazarov O, Binder LI, Morfini GA. Axonal degeneration in Alzheimer's disease: when signaling abnormalities meet the axonal transport system. Exp Neurol 2012; [Epub ahead of print].

Keihaninejad S, Ryan N, Malone I, Leung K, Hyare H, Ourselin S, et al. Automated segmentation of the thalamus for measurement of MR diffusion indices: evaluation and application to familial Alzheimer's disease [abstract]. Alzheimer's Demen 2011; 7: 4, S50.

Keihaninejad S, Zhang H, Ryan N, Malone I, Frost C, Cardoso M, et al. White matter tract changes in mild-to-moderate Alzheimer's disease revealed by tensor-based registration analysis of diffusion tensor imaging [abstract]. Alzheimer's Dement 2012a; 8: 4, P31.

Keihaninejad S, Ryan NS, Malone IB, Modat M, Cash D, Ridgway GR, et al. The importance of group-wise registration in Tract Based Spatial Statistics study of neurodegeneration: a simulation study in Alzheimer's disease. PLoS One 2012b; 7: e45996.

Klunk WE, Engler H, Nordberg A, Wang Y, Blomqvist G, Holt DP, et al. Imaging brain amyloid in Alzheimer's disease with Pittsburgh Compound-B. Ann Neurol 2004; 55: 306–19.

Klunk WE, Price JC, Mathis CA, Tsopelas ND, Lopresti BJ, Ziolko SK, et al. Amyloid deposition begins in the striatum of presenilin-1 mutation carriers from two unrelated pedigrees. J Neurosci 2007; 27: 6174–84.

Knight WD, Kim LG, Douiri A, Frost C, Rossor MN, Fox NC. Acceleration of cortical thinning in familial Alzheimer's disease. Neurobiol Aging 2011a; 32: 1765–73.

Knight WD, Okello AA, Ryan NS, Turkheimer FE, Rodríguez Martinez de Llano S, Edison P, et al. Carbon-11-Pittsburgh compound B positron emission tomography imaging of amyloid deposition in presenilin 1 mutation carriers. Brain 2011b; 134: 293–300.

Lee GJ, Lu PH, Medina LD, Rodriguez-Agudelo Y, Melchor S, Coppola G, et al. Regional brain volume differences in symptomatic and presymptomatic carriers of familial Alzheimer's disease mutations. J Neurol Neurosurg Psychiatry 2013; 84: 154–62.

Leung KK, Barnes J, Modat M, Ridgway GR, Bartlett JW, Fox NC, et al. Brain MAPS: an automated, accurate and robust brain extraction technique using a template library. Neuroimage 2011; 55: 1091–108.

Leung KK, Barnes J, Ridgway GR, Bartlett JW, Clarkson MJ, Macdonald K, et al. Automated cross-sectional and longitudinal hippocampal volume measurement in mild cognitive impairment and Alzheimer's disease. Neuroimage 2010; 51: 1345–59.

Lifshitz J, Kelley BJ, Povlishock JT. Perisomatic thalamic axotomy after diffuse traumatic brain injury is associated with atrophy rather than cell death. J Neuropathol Exp Neurol 2007; 66: 218–29.

Mattson MP, Magnus T. Ageing and neuronal vulnerability. Nat Rev Neurosci 2006; 7: 278–94.

McKinstry RC, Mathur A, Miller JH, Ozcan A, Snyder AZ, Schefft GL, et al. Radial organization of developing preterm human cerebral cortex revealed by non-invasive water diffusion anisotropy MRI. Cereb Cortex 2002; 12: 1237–43.

Middleton FA, Strick PL. Basal ganglia output and cognition: evidence from anatomical, behavioral, and clinical studies. Brain Cogn 2000; 42: 183–200.

Modat M, Ridgway GR, Taylor ZA, Lehmann M, Barnes J, Hawkes DJ, et al. Fast free-form deformation using graphics processing units. Comput Methods Programs Biomed 2010; 98: 278–84.

Mori S, Wakana S, Nagae-Poetscher L, van Zijl P. MRI atlas of human white matter. Amsterdam. Elsevier, 2005.

Neave N, Nagle S, Aggleton JP. Evidence for the involvement of the mammillary bodies and cingulum bundle in allocentric spatial processing by rats. Eur J Neurosci 1997; 9: 941–55.

Nelson O, Supnet C, Liu H, Bezprozvanny I. Familial Alzheimer's disease mutations in presenilins: effects on endoplasmic reticulum calcium homeostasis and correlation with clinical phenotypes. J Alzheimers Dis 2010; 21: 781–93.

Nestor PJ, Fryer TD, Smielewski P, Hodges JR. Limbic hypometabolism in Alzheimer's disease and mild cognitive impairment. Ann Neurol 2003; 54: 343–51.

O'Dwyer L, Lamberton F, Matura S, Tanner C, Scheibe M, Miller J, et al. Reduced hippocampal volume in healthy young ApoE4 carriers: an MRI study. PLoS One 2012; 7: e48895.

O'Riordan S, McMonagle P, Janssen JC, Fox NC, Farrell M, Collinge J, et al. Presenilin-1 mutation (E280G), spastic paraparesis, and cranial MRI white-matter abnormalities. Neurology 2002; 59: 1108–10.

Olabarria M, Noristani HN, Verkhratsky A, Rodriguez JJ. Concomitant astroglial atrophy and astrogliosis in a triple transgenic animal model of Alzheimer's disease. Glia 2010; 58: 831–8.

Ourselin S, Roche A, Subsol G, Pennec X, Ayache N. Reconstructing a serial structure from serial histological sections. Image Vision Comput 2001; 19: 25–31.

Oyanagi K, Takahashi H, Wakabayashi K, Ikuta F. Selective involvement of large neurons in the neostriatum of Alzheimer's disease and senile dementia: a morphometric investigation. Brain Res 1987; 411: 205–11.

Pappata S, Levasseur M, Gunn RN, Myers R, Crouzel C, Syrota A, et al. Thalamic microglial activation in ischemic stroke detected in vivo by PET and [11C]PK1195. Neurology 2000; 55: 1052–4.

Pedro T, Weiler M, Yasuda CL, D'Abreu A, Damasceno BP, Cendes F, et al. Volumetric brain changes in thalamus, corpus callosum and medial temporal structures: mild Alzheimer's disease compared with amnestic mild cognitive impairment. Dement Geriatr Cogn Disord 2012; 34: 149–55.

Price JL, Morris JC. Tangles and plaques in nondemented aging and 'preclinical' Alzheimer's disease. Ann Neurol 1999; 45: 358–68.

Ramlackhansingh AF, Brooks DJ, Greenwood RJ, Bose SK, Turkheimer FE, Kinnunen KM, et al. Inflammation after trauma: microglial activation and traumatic brain injury. Ann Neurol 2011; 70: 374–83.

Reiman EM, Langbaum JB, Tariot PN. Alzheimer's prevention initiative: a proposal to evaluate presymptomatic treatments as quickly as possible. Biomark Med 2010; 4: 3–14.

Reiman EM, Quiroz YT, Fleisher AS, Chen K, Velez-Pardo C, Jimenez-Del-Rio M, et al. Brain imaging and fluid biomarker analysis in young adults at genetic risk for autosomal dominant Alzheimer's disease in the presenilin 1 E280A kindred: a case-control study. Lancet Neurol 2012; 11: 1048–56.

Ridgway G, Barnes J, Pepple T, Fox N. Estimation of total intracranial volume; a comparison of methods [abstract]. Alzheimer's Demen 2011; 7: S62.

Ridha BH, Barnes J, Bartlett JW, Godbolt A, Pepple T, Rossor MN, et al. Tracking atrophy progression in familial Alzheimer's disease: a serial MRI study. Lancet Neurol 2006; 5: 828–34.

Ringman JM, O'Neill J, Geschwind D, Medina L, Apostolova LG, Rodriguez Y, et al. Diffusion tensor imaging in preclinical and presymptomatic carriers of familial Alzheimer's disease mutations. Brain 2007; 130: 1767–76.

Rodriguez JJ, Witton J, Olabarria M, Noristani HN, Verkhratsky A. Increase in the density of resting microglia precedes neuritic plaque formation and microglial activation in a transgenic model of Alzheimer's disease. Cell Death Dis 2010; 1: e1.

Ryan NS, Rossor MN. Correlating familial Alzheimer's disease gene mutations with clinical phenotype. Biomark Med 2010; 4: 99–112.

Schmahmann JD. Vascular syndromes of the thalamus. Stroke 2003; 34: 2264–78.

Smith CD, Chebrolu H, Andersen AH, Powell DA, Lovell MA, Xiong S, et al. White matter diffusion alterations in normal women at risk of Alzheimer's disease. Neurobiol Aging 2010; 31: 1122–31.

Smith SM, Jenkinson M, Johansen-Berg H, Rueckert D, Nichols TE, Mackay CE, et al. Tract-based spatial statistics: voxelwise analysis of multi-subject diffusion data. Neuroimage 2006; 31: 1487–505.

Smith SM, Nichols TE. Threshold-free cluster enhancement: addressing problems of smoothing, threshold dependence and localisation in cluster inference. Neuroimage 2009; 44: 83–98.

Song SK, Sun SW, Ju WK, Lin SJ, Cross AH, Neufeld AH. Diffusion tensor imaging detects and differentiates axon and myelin degeneration in mouse optic nerve after retinal ischemia. Neuroimage 2003; 20: 1714–22.

Spain A, Daumas S, Lifshitz J, Rhodes J, Andrews PJ, Horsburgh K, et al. Mild fluid percussion injury in mice produces evolving selective axonal pathology and cognitive deficits relevant to human brain injury. J Neurotrauma 2010; 27: 1429–38.

Stebbins GT, Murphy CM. Diffusion tensor imaging in Alzheimer's disease and mild cognitive impairment. Behav Neurol 2009; 21: 39–49.

Sun SW, Song SK, Harms MP, Lin SJ, Holtzman DM, Merchant KM, et al. Detection of age-dependent brain injury in a mouse model of brain amyloidosis associated with Alzheimer's disease using magnetic resonance diffusion tensor imaging. Exp Neurol 2005; 191: 77–85.

Tovar-Moll F, Evangelou IE, Chiu AW, Richert ND, Ostuni JL, Ohayon JM, et al. Thalamic involvement and its impact on clinical disability in patients with multiple sclerosis: a diffusion tensor imaging study at 3T. AJNR Am J Neuroradiol 2009; 30: 1380–6.

Van der Werf YD, Jolles J, Witter MP, Uylings HB. Contributions of thalamic nuclei to declarative memory functioning. Cortex 2003; 39: 1047–62.

Wang Y, Gupta A, Liu Z, Zhang H, Escolar ML, Gilmore JH, et al. DTI registration in atlas based fiber analysis of infantile Krabbe disease. Neuroimage 2011; 55: 1577–86.

Warfield SK, Zou KH, Wells WM. Simultaneous truth and performance level estimation (STAPLE): an algorithm for the validation of image segmentation. IEEE Trans Med Imaging 2004; 23: 903–21.

Warren JD, Rohrer JD, Hardy J. Disintegrating brain networks: from syndromes to molecular nexopathies. Neuron 2012; 73: 1060–2.

Warrington EK, Agnew SK, Kennedy AM, Rossor MN. Neuropsychological profiles of familial Alzheimer's disease associated with mutations in the presenilin 1 and amyloid precursor protein genes. J Neurol 2001; 248: 45–50.

Weiskopf N, Lutti A, Helms G, Novak M, Ashburner J, Hutton C. Unified segmentation based correction of R1 brain maps for RF transmit field inhomogeneities (UNICORT). Neuroimage 2011; 54: 2116–24.

Wiegell MR, Tuch DS, Larsson HBW, Wedeen VJ. Angular differentiation of thalamic nuclei by quantitative DTI. Proc Int Soc Mag Reson Med 2000; 8: 481.

Wilson S, Raghupathi R, Saatman KE, MacKinnon MA, McIntosh TK, Graham DI. Continued *in situ* DNA fragmentation of microglia/macrophages in white matter weeks and months after traumatic brain injury. J Neurotrauma 2004; 21: 239–50.

Xuereb JH, Perry RH, Candy JM, Perry EK, Marshall E, Bonham JR. Nerve cell loss in the thalamus in Alzheimer's disease and Parkinson' disease. Brain 1991; 114 (Pt 3): 1363–79.

Zhang H, Yushkevich PA, Alexander DC, Gee JC. Deformable registration of diffusion tensor MR images with explicit orientation optimization. Med Image Anal 2006; 10: 764–85.

Zhang H, Schneider T, Wheeler-Kingshott CA, Alexander DC. NODDI: practical *in vivo* neurite orientation dispersion and density imaging of the human brain. Neuroimage 2012; 61: 1000–16.